

Towards Spherical Robots For Mobile Mapping In Human Made Environments*

Fabian Arzberger and Anton Bredenbeck, Jasper Zevering, Dorit Borrmann, Andreas Nüchter

*Informatics VII: Robotics and Telematics, Julius-Maximilians-University Würzburg, Germany
e-mail: dorit.borrmann@uni-wuerzburg.de*

Abstract

Spherical robots are a format that hasn't been thoroughly explored for the application of mobile mapping. In contrast to other designs it provides some unique advantages. Among those are a protective spherical shell which protects internal sensors and actuators from possible harsh environments as well as an inherent rotation for locomotion that enables measurements in all directions. Mobile mapping always requires a high-precise pose knowledge to obtain consistent and correct environment maps. This is typically be done by a combination of external reference sensors such as GNSS measurements and inertial measurements, or by post processing the data and registering the different measurements to each other. In indoor environments the GNSS reference is not an option, hence many mobile mapping applications turn to the second option. An advantage of indoor environments is, that human made environments usually have a certain structure, such as parallel planes and right angles. We propose a registration procedure that exploits this structure by minimizing the distance of measured points to a corresponding plane. Further we evaluate the procedure on a simulated dataset of an ideal corridor as well as in experimentally acquired datasets with different motion profiles. We show that we nearly reproduce the ground truth for the simulated dataset and improve the average point-to-point distance to a reference scan in the experimental dataset. The presented algorithms are required to work completely autonomous.

Keywords: Mobile Mapping, SLAM, Spherical Robot

2021 MSC: 00-01, 99-00

1. Introduction

Today's robots for mobile mapping come in all shapes and sizes. The state of the art for urban environments are laser scanners mounted to cars. Smaller robotic systems are particularly used when cars no longer have access. Examples for this are human operated systems such as Zebedee [?], a Hokuyo scanner on a spring, VILMA [1], a rolling FARO scanner, RADLER [2], a 2D laser scanner mounted to a unicycle, or a backpack mounted "personal laser scanning system" as in [3]. Recently more and more autonomous systems gained maturity. A stunning example is Boston Dynamics' quadruped "Spot" that autonomously navigates and maps human environments [4]. Also the mobile mapping approaches implemented on the ANYmal platform such as [5] were very successful. Of all these formats, one hasn't been explored thoroughly in the scientific community: The spherical mobile mapping robot. Yet this provides some very promising advantages over the other formats. For one, the locomotion of a spherical robot inherently results in a rotation. That way a sensor fixed inside the spherical structure will cover the entire environment, given the required locomotion without the need for additional actuators for the sensors. This requires

a solution for the spherical simultaneous localization and mapping (SLAM) problem given the six degrees of freedom of the robot. Secondly a spherical shell, that encloses all sensors protects these from possible hazardous environments. For example, any dust that deteriorates sensors or actuators when settling at sensitive locations is stopped by a shell. This is be particularly useful for unknown and dangerous environments. E.g., for space applications this is also proposed in the DAEDALUS study [6], a spherical robot that is to be lowered into a lunar cave and create a 3D map of the environment. The authors choose this format as the present moon regolith is known to damage instruments and other components.

This paper proposes to use such a spherical robot for mobile mapping man made environments. In such environments one advantage are architectural shapes following standard conventions arising from tradition or utility, i.e., there are many flat surfaces such as walls, floors etc. that are sensed. Exploiting this fact yields more opportunities for registration as point-to-plane correspondences can be used. The proposed registration method minimizes the distances of each point to its corresponding plane as objective function. The method is evaluated on a simulated dataset as well as on experimentally acquired datasets.

*To abide the FAIR-Principles of science, all data and code used to produce the results are given in this github repository.

2. State Of The Art

2.1. Spherical SLAM

Up to the best of our knowledge, SLAM with spherical robots and laser scanners was not done before, while there exists camera based approaches [7]. However, laser-based SLAM algorithms for motions in six degrees of freedom (DoF) have been thoroughly studied. For outdoor environments [8] provides a first baseline. Adding a heuristic for closed loop detection and a global relaxation Borrmann et al. yield highly precise maps of the scanned environment [9]. Zhang et al. propose a real-time version of the SLAM algorithm in [10]. They achieve the performance at a lower computational load by dividing the SLAM algorithm into two different algorithms: one performing odometry at a high frequency but low fidelity and another running at a lower frequency performing fine matching and registration of the point clouds. The more recently Dröschel et al. also proposes an online method using a novel combination of a hierarchical graph structure with local multi-resolution maps to overcome problems due to sparse scans [11].

Since these approaches are based on point-to-point correspondences they require rather high point density to achieve precise registration. For low-cost LiDARs this implies a slow motion and long integration time. Further, none of the approaches exploit the structure inherent to man-made environments, hence missing out on possible advantages.

2.2. Point Cloud Registration Using Plane Based Correspondences

The de-facto standard for many SLAM algorithms is the Iterative-Closest-Point (ICP) algorithm [12] that employs point-to-point correspondences using closest points, as the name suggests. To overcome the requirements on point-density imposed by the point-to-point correspondences instead other correspondences are used. In man made environments planes are abundantly available, and hence provide an attractive base for correspondences. Förster et al. use this property of man made environment successfully in [13]. They register point clouds using plane-to-plane correspondences and include uncertainty measures for the detected planes as well as the estimated motion. Thereby, they propose a costly exact algorithm and cheaper approximations that yield high quality maps. Favre et al. [14] use point-to-plane correspondences after preprocessing the point clouds using plane-to-plane correspondences to successfully register two scans with each other.

Both approaches use plane-to-plane correspondences to pre-register the scans. However for pre-registration the classical point-to-point registration is also very effective. One advantage that point-to-point correspondences have over plane-to-plane correspondences is, that they do not require a long stop in each pose. For plane-to-plane correspondences this is required to gather enough data to measure planes in each individual scan robustly. The result-

ing scan procedure is stop-scan-and-go. In particular for the application of a spherical robot this standstill in each pose cannot be guaranteed or even approximated making continuous-time approaches using point-to-plane correspondences the method of choice.

In the following we propose this combination of point-to-point based pre-registration followed by a point-to-plane based optimization.

3. Registration Algorithm

We start with transforming each line scan into the project coordinate system , which is defined by the pose of the first acquired line scan. With line scan, we mean the smallest chunk of range data, we obtain from the scanner device driver. In case of a SICK LMS1xx it is a line and in case of a Livox scanner it has a flower shape. More details are provided in the following sections. For map improvement the individual scans need to be registered to another. We propose an algorithm that consist of multiple steps outlined in algorithm 1. Based on ideas described in [15] we first rigidly register the scans and then further improve the overall map by exploiting the fact that man made environments often consist of planes. We then find the planes in the pre-registered point-cloud and then optimize the poses associated with the scans to minimize the distance of all points to their respective planes.

Algorithm 1: Registration algorithm for man-made environments

Result: A corrected map

1. Rigidly register the scans;
 2. Extract planes from the registered map;
 3. Further improve map by solving the optimization that minimizes the distance of all points to their respective planes;
-

3.1. Plane Extraction

After having done the rigid registration the scans are aligned well-enough to make statements about the potential planes in the environment. To find the planes in the environment a Hough transform with an accumulator ball as described in [16] is used. In the next subsection the Hesse-normal form of the plane is required. For an ideal plane the distance parameter $\rho_{\mathcal{P}_i}$ is computed via $\mathbf{n}_{\mathcal{P}_i} \cdot \mathbf{x}_i$, where \mathbf{x}_i is an arbitrary point on the plane. To find this point we first define a convex hull that encloses the plane. It is defined by the points that lie on the plane with the furthest distance to one another. We then choose the center point of the convex hull of the plane as \mathbf{x}_i .

3.2. Point-to-Plane Correspondences

There are many ways of finding correspondences between points and planes. However, even with the result

not being perfect, we assume already globally registered scans, which is why a simplistic algorithm is sufficient: For each plane, consider adding a correspondence for all points that are closer to the plane than a threshold ϵ . Depending on the threshold value, some points now have multiple correspondences if their distance to multiple planes is less than ϵ . We then simply omit all points that have correspondences to multiple planes from the optimizations, to avoid introducing errors due to the plane ambiguity.

Add section about the local plane, k-means normal based region growing aka clustering for point2plane correspondences. Basically, if a point is correspondence to a global plane than all other points that lie on its local plane should be too. The local plane is constructed by region growing, i.e. if the difference in normal and the distance of the points are close enough they are clustered to one local plane.

3.3. Optimization

Assuming we now know the Hesse-normal form of all planes and all points that are assigned to these planes, we register the points to have a minimal distance to their respective planes. The transformation $T(\mathbf{p}_k)$ of each point \mathbf{p}_k with respect to a 6 DoF motion is described in homogeneous coordinates using the roll-pitch-yaw ($\varphi - \vartheta - \psi$) Tait-Brian angles as in [17]. Transforming the result back from homogeneous coordinates and using C_k and S_k to denote the cosine and sine of the angle in the subscript yields:

$$T(\mathbf{p}_k) = \begin{bmatrix} xC_\vartheta C_\psi - yC_\varphi S_\psi + zS_\vartheta + t_x \\ x(C_\varphi S_\psi + C_\psi S_\varphi S_\vartheta) + y(C_\varphi C_\psi - S_\varphi S_\vartheta S_\psi) - zC_\vartheta S_\varphi + t_y \\ x(S_\varphi S_\psi - C_\varphi C_\psi S_\vartheta) + y(C_\psi S_\varphi + C_\varphi S_\vartheta S_\psi) + zC_\varphi C_\vartheta + t_z \end{bmatrix} \quad (1)$$

From this we define the function $D(\varphi, \vartheta, \psi, t_x, t_y, t_z, \mathbf{p}_k)$ that computes the distance of a point \mathbf{p}_k to its corresponding plane \mathcal{P}_i . Omitting the arguments of the function for simplicity:

$$\begin{aligned} D &= T(\mathbf{p}_k) \cdot \mathbf{n}_{\mathcal{P}_i} \\ &= n_{\mathcal{P}_i}^x (xC_\vartheta C_\psi - yC_\varphi S_\psi + zS_\vartheta + t_x) \\ &\quad + n_{\mathcal{P}_i}^y (x(C_\varphi S_\psi + C_\psi S_\varphi S_\vartheta) \\ &\quad + y(C_\varphi C_\psi - S_\varphi S_\vartheta S_\psi) - zC_\vartheta S_\varphi + t_y) \\ &\quad + n_{\mathcal{P}_i}^z (x(S_\varphi S_\psi - C_\varphi C_\psi S_\vartheta) \\ &\quad + y(C_\psi S_\varphi + C_\varphi S_\vartheta S_\psi) + zC_\varphi C_\vartheta + t_z) \\ &\quad - \rho_{\mathcal{P}_i} \end{aligned} \quad (2)$$

This distance function is what we want to minimize for all points and their respective planes. Hence the error function E is chosen as follows:

$$E = \sum_{\forall \mathcal{P}_i} \sum_{\mathbf{p}_k \in \mathcal{P}_i} \|D(\varphi, \vartheta, \psi, t_x, t_y, t_z, \mathbf{p}_k)\|_2^2 \quad (3)$$

Its gradient follows then immediately:

$$\nabla E = \sum_{\forall \mathcal{P}_i} \sum_{\mathbf{p}_k \in \mathcal{P}_i} \left[\frac{\partial}{\partial \varphi} E \quad \frac{\partial}{\partial \vartheta} E \quad \frac{\partial}{\partial \psi} E \quad \frac{\partial}{\partial t_x} E \quad \frac{\partial}{\partial t_y} E \quad \frac{\partial}{\partial t_z} E \right]^T \quad (4)$$

$$\Rightarrow \nabla E = \sum_{\forall \mathcal{P}_i} \sum_{\mathbf{p}_k \in \mathcal{P}_i} 2D(\mathbf{p}_k) [\nabla E_\varphi \quad \nabla E_\vartheta \quad \nabla E_\psi \quad n_{\mathcal{P}_i}^x \quad n_{\mathcal{P}_i}^y \quad n_{\mathcal{P}_i}^z]^T \quad (5)$$

Where

$$\begin{aligned} \nabla E_\varphi &= n_{\mathcal{P}_i}^x y S_\varphi S_\psi \\ &\quad + n_{\mathcal{P}_i}^y (x[-S_\varphi S_\psi + C_\varphi C_\psi S_\vartheta] \\ &\quad + y[-S_\varphi C_\psi - C_\varphi S_\vartheta S_\psi] \\ &\quad - zC_\varphi C_\vartheta) \\ &\quad + n_{\mathcal{P}_i}^z (x[C_\varphi S_\psi + C_\varphi C_\psi S_\vartheta] \\ &\quad + y[C_\varphi C_\psi - S_\varphi S_\vartheta S_\psi] \\ &\quad - zS_\varphi C_\vartheta) \end{aligned} \quad (6)$$

$$\begin{aligned} \nabla E_\vartheta &= n_{\mathcal{P}_i}^x (-xS_\vartheta C_\psi + zC_\vartheta) \\ &\quad + n_{\mathcal{P}_i}^y (xC_\psi S_\varphi C_\vartheta - yS_\varphi C_\vartheta S_\psi + zS_\vartheta S_\varphi) \\ &\quad + n_{\mathcal{P}_i}^z (-xC_\varphi C_\psi C_\vartheta + yC_\varphi C_\vartheta S_\psi - zC_\varphi S_\vartheta) \end{aligned} \quad (7)$$

$$\begin{aligned} \nabla E_\psi &= n_{\mathcal{P}_i}^x (-xC_\vartheta S_\psi - yC_\varphi C_\psi) \\ &\quad + n_{\mathcal{P}_i}^y (x[C_\varphi C_\psi - S_\varphi S_\vartheta S_\psi] + y[-C_\varphi S_\psi - S_\varphi S_\vartheta C_\psi]) \\ &\quad + n_{\mathcal{P}_i}^z (x[S_\varphi C_\psi + C_\varphi S_\psi S_\vartheta] + y[-S_\psi S_\varphi + C_\varphi S_\vartheta C_\psi]) \end{aligned} \quad (8)$$

and $\mathbf{\Pi} = [\varphi \quad \vartheta \quad \psi \quad t_x \quad t_y \quad t_z]^T$.

As the gradient is well-defined we minimize the error function with any gradient based method. The commonly used, well-known stochastic gradient descent (SDG) algorithm computes

$$\mathbf{\Pi}_{k+1} = \mathbf{\Pi}_k - \alpha \nabla E \quad (9)$$

To accelerate convergence and to improve the found solution further modifications are made.

Since we have vastly different effects on the error function by each dimension, the first consideration for improving the SDG is the following: Typically, changes in orientation, i.e., the first three elements of the gradient vector $\frac{\partial}{\partial \varphi} E$, $\frac{\partial}{\partial \vartheta} E$, and $\frac{\partial}{\partial \psi} E$, have much more impact on the error function than a change in position. This is intuitively explained since translating the scan makes the error grow linearly for all points. However, when rotating the scan, points with a larger distance to the robot are moved drastically, leading to a higher sensibility on the error function. For this reason, the α applied on orientation has to be much smaller than the α applied on the position. It becomes obvious that α needs to be extended into vector form, $\boldsymbol{\alpha}$, therefore weighting each dimension differently.

Another consideration to speed up SDG is to adaptively recalculate $\boldsymbol{\alpha}$ for each iteration. We employ and modify ADADELTA as a technique to do so, which is described in detail in [18]. The main idea is the following: It extends the SDG algorithm by two terms. First, an

exponentially decaying average of past gradients, which is recursively defined as

$$\mathbf{G}_{k+1} = \rho \mathbf{G}_k + (1 - \rho) \nabla E^2 \quad (10)$$

and second, an exponentially decaying average of past changes, which is defined as

$$\mathbf{X}_{k+1} = \rho \mathbf{X}_k + (1 - \rho) \boldsymbol{\alpha} \nabla E^2 \quad (11)$$

where $\rho \leq 1$ is a decay constant, typically close to 1. The root mean squared (RMS) of these quantities are

$$RMS[\mathbf{G}]_k = \sqrt{\mathbf{G}_k + \epsilon} \quad (12)$$

and

$$RMS[\mathbf{X}]_k = \sqrt{\mathbf{X}_k + \epsilon} \quad (13)$$

where $\epsilon > 0$ is a very small constant, typically close to 0. It will prevent dividing by zero in the recalculation of $\boldsymbol{\alpha}$, which is as follows:

$$\boldsymbol{\alpha}_k = \frac{RMS[X]_{k-1}}{RMS[G]_k} \quad (14)$$

For our particular application ADADELTA behaves a little too aggressively. Despite giving a good measure on how to adapt $\boldsymbol{\alpha}$, the algorithm sometimes overshoots, and convergence doesn't happen. Therefore, we employ another scaling factor, typically not found in ADADELTA, extending eq. (14) to:

$$\boldsymbol{\alpha}_k = \boldsymbol{\alpha}_0 \cdot \frac{RMS[X]_{k-1}}{RMS[G]_k} \quad (15)$$

where $\boldsymbol{\alpha}_0$ holds the scaling factors for each dimension.

Finally, the SDG model is improved using eq. (15) and extends to

$$\boldsymbol{\Pi}_{k+1} = \boldsymbol{\Pi}_k - \boldsymbol{\alpha}_0 \frac{RMS[X]_{k-1}}{RMS[G]_k} \cdot \nabla E \quad (16)$$

Using this algorithm once after finding correspondences from points to planes leads to convergence to a local minimum, which often isn't an optimal solution. Even if the number of iterations is dramatically increased, no better solution than the local minimum is found. That is, unless you consider updating the correspondence model after i^{220} iterations of gradient descent. Re-assigning point-to-plane correspondences this way k times, and if k is chosen large enough, it leads to an optimal solution after maximum $n = k \cdot i$ iterations of gradient descent.

3.4. Further Optimizations of the Algorithm

The algorithm was extended by two further optimizations which are useful in different scenarios.

Firstly, we introduce a lock on some dimensions from being optimized by setting the corresponding α_i to zero. Although 6D optimization generally works, reducing the

optimization space is particularly useful if the source of error in the system is known and a model exists. That way, e.g. a point cloud from a terrestrial laserscanner that experiences irregularities in its spinning mirror is registered by optimizing only over the axis of rotation as no other movement is to be expected.

Secondly we employ a continuous iteration, where the scans are processed sequentially. This is especially useful for mobile systems, where pose error accumulates due to increasing tracking uncertainties. The assumption is that the error in one scan is also present in the next scan, plus some unknown new error. We eliminate the error from scan m which is also present in scan $m + 1$ by applying the pose change from scan m , $\boldsymbol{\Pi}_{n,m} - \boldsymbol{\Pi}_{0,m}$ after n gradient descent iterations, to scan $m + 1$, before restarting gradient descent. To quantify the quality of the proposed registration method, it is tested on simulated as well as on real world data.

4. Simulation

For the simulated data we implemented a noisy world-robot-sensor model. We are simulating a LIOVOX-Mid100 [19] laser scanner with customizable noise level on the range measurements inside a robot with different motion capabilities, subject to noise in its pose estimation. This yields scan results similar to the ones obtained in the real world.

4.1. Range Noise Model

Most real laser scanners are subjected to range measurement noise that is proportional to the measured range. Therefore the simulated sensors are as well. To achieve this we sample a noise percentage n_P from some normal distribution $\mathcal{N}(\mu, \sigma^2)$. The resulting range r given the true range r_t is then

$$r = r_t(1 + n_P) \quad (17)$$

For each measurement ray the noise percentage is sampled independently.

4.2. Pose Estimation Noise Model

For the pose measurement one cannot simply add white noise to the current pose estimate as this does not capture the integration error which is common among inertial measurement units (IMU). Therefore we assume a disturbance torque about the two axes that lie in the ground plane. This is equivalent to a case, where a slightly shifted ground plane or an unbalanced locomotion system of the robot is present.

Accordingly, a spherical robot that is assumed to be translating exactly along one axis by rotation exactly about one other axis at an angular velocity ω experiences random disturbance torques at each time instant that accelerate the sphere's rotation about the respective axes. This additional motion is determined by integrating the disturbance

torques which are sampled from some normal distribution $n_\phi, n_\psi \in \mathcal{N}(\mu, \sigma^2)$ each. The pose update in the discrete simulation is therefore given by:

$$\begin{bmatrix} \varphi \\ \vartheta \\ \psi \\ x \\ y \\ z \end{bmatrix}_{k+1} = \begin{bmatrix} \varphi \\ \vartheta \\ \psi \\ x \\ y \\ z \end{bmatrix}_k + \underbrace{\begin{bmatrix} 1 \\ 0 \\ 0 \\ R \\ 0 \\ 0 \end{bmatrix}}_{\text{Difference in angular velocity}} \omega \Delta t + \Delta t \sum_{i=0}^k \begin{bmatrix} n_\varphi[i] \Delta t \\ 0 \\ n_\psi[i] \Delta t \\ 0 \\ 0 \\ 0 \end{bmatrix} \quad (18)$$

Assuming intended locomotion along the z -axis and unintended locomotion along the x -axis where R is the sphere radius. No movement upwards is possible since the robot moves on a flat ground, hence the entry is zero.

4.3. Simulated Datasets

Figure 1 shows a noise free trajectory through a simulated environment as well as a trajectory with noisy sensors. In the noise-free case, the trajectory slightly bends in the direction of disturbance torque sideways while also varying in velocity in the intended direction of travel. In the noisy case the ideal straight trajectory is assumed, hence the planes enclosing the room are sensed multiple times. In particular we see that the trajectory of the robot leads through one of the sensed planes. Also, the further the sensed points are the noisier they appear, which is consistent with the larger influence of the pose error at higher distances.

5. Experimental Setup

Our algorithm was also tested on a number of real-world datasets that adhere to different motion profiles and laser scanners with different scanning patterns.

5.1. Floating Sphere

The first dataset is collected by a line scanner, in particular a SICK LMS141 industrial scanner, inside a sphere of a diameter of 20 cm that lies on a floating desk, which is air-pressurized, such that the sphere is hovering. On this floating desk the sphere can rotate freely about all axis while being fixed in position. Hence, in this experiment the optimization space can be reduced to a rotation but also the motion is required to obtain a 3D model from the 2D laser scanner. The sphere is equipped with a low-cost IMU, i.e., a PhidgetSpatial Precision 3/3/3, to estimate the initial orientation.

Figure 2 shows the experimental setup. TThe left column of figure 6 shows the pre-registered resulting point cloud . We see, that the point cloud is rather noisy and in particular the walls are sensed multiple times, hence appearing very blurry.

5.2. RADLER

The second dataset is recorded using the RADLER system as described in [2]. While not a spherical robot, this system shows many similarities with respect to its motion with a spherical robot. The system was manually steered along a squared set of hallways that loop back to the initial starting point inside the old mathematics building at the University of Würzburg (denoted “The Circle” in [2]).

Figure 3 shows the system setup as well as the resulting point cloud. We see that with continuing measurement time the drift increases and the hallways are sensed multiple times with a clear offset to each other.

5.3. Descend Sphere REMOVE THIS SECTION

This was recorded using a LIVOX-Mid 100 laser scanner mounted inside a transparent shell. The robot contained three Phidget 3/3/3 Spatial IMUs and was attached to a 50 m tether cable that was rolled on a spool which in turn was connected to a angular encoder. From these sensors we obtained orientation information as well as height information. The setup was then brought into a high indoor building (Firefighter School in Würzburg) where the system was manually descended from a balcony scanning the building interior. The robot covered a distance of approximately 22 m in about 402 s. Additionally the building was scanned using a terrestrial laser scanner to provide a reference. The measurements were then rigidly corrected before applying our plane based correction. Figure 4 shows the acquired 3D point clouds and the experimental setup.

6. Results

6.1. Simulated Results

The plane-based registration is applied to the simulated dataset with noisy pose and range measurements (cf. Figure 1) without further processing. Assuming this represents a coarsely pre-registered 3D point cloud the distances to the ground truth were evaluated before and after the plane-based registration. Figure 5 shows the different point-to-point distances.

Before the registration the corridor is only represented acceptably in the front part. The further into the corridor, i.e. the longer the robot accumulates error, the more imprecise the date becomes. Finally we see that a large portion of the data even exceeds either the 1 m error, contributing to the large spike in the histogram or even the 2 m error limit thus, being cut from the representation. After registration, we see that, qualitatively, the ideal corridor was nearly restored from the noisy data. In particular a very large portion (95%) have less than 17 cm distances. Further the square and straight shape of the corridor is restored well and especially the large spike at errors of greater than 1 m is remove. Any such errors tend to occur at the back and the front of the corridor where the measured range is the largest, hence has the largest contribution of the range error.

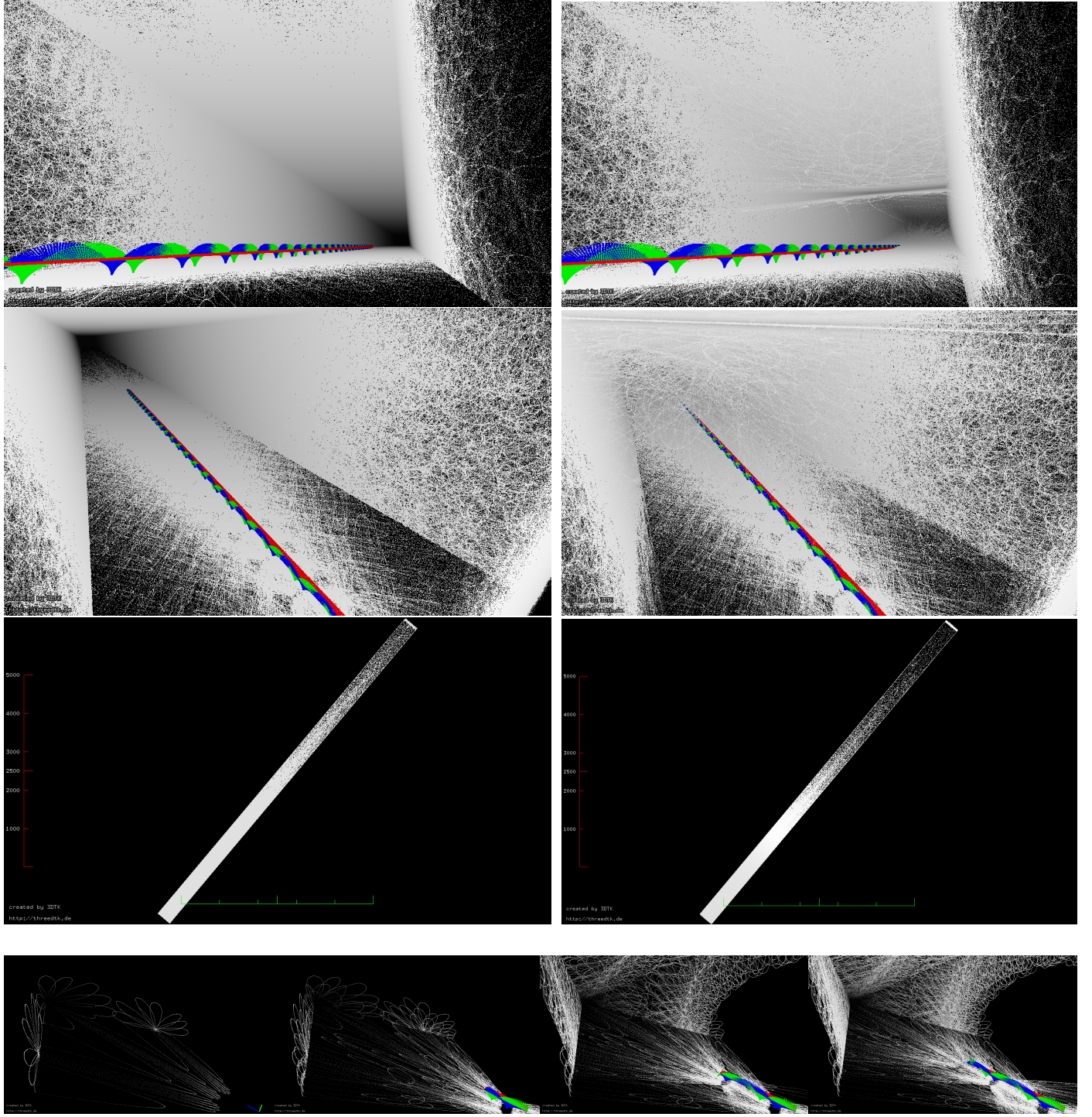


Figure 1: Two simulated datasets of a long hallway of size $4 \text{ m} \times 3 \text{ m} \times 100 \text{ m}$. Ideal noise free (left), noisy pose ($\mathcal{N}_\varphi = \mathcal{N}_\psi(\mu = 0.0001, \sigma = 0.00001)$) and noisy range measurements ($\mathcal{N}_r(\mu = 0, \sigma = 0.001)$) (right). Below: Initial sequence of the simulation of the ideal dataset showing the simulated motion of the robot.

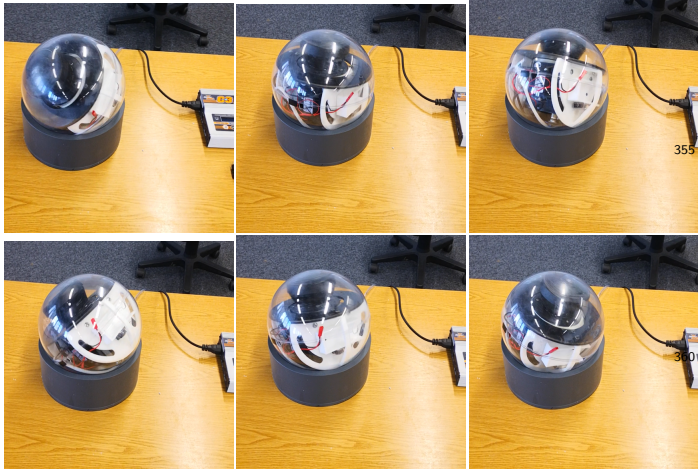


Figure 2: Data acquisition using floating sphere. We show a sequence of orientations the sphere assumes.

6.2. Floating Sphere Results

Figure 6 shows the results obtained after employing³⁶⁵ the plane base registration on the dataset acquired by the floating sphere. After the registration the walls of the room are significantly more prominent in the point-cloud. In particular the noise in the top left corner of the top³⁷⁰ view (cf. figure 6) has been visibly reduced. Further, the noise around the walls is notably reduced as the points are moved on the plane.

However, some imprecisions remain. At the same location a few points cannot be matched to the plane as they are clustered with some other points that are bound to a different pose. Hence this error stems from the imprecise³⁸⁰ interpolation in between scans.

More comments here

6.3. RADLER Results

6.4. Experimental Results REMOVE THIS SECTION

For the experimentally acquired datasets a similar procedure is followed. The main difference being, that the³⁹⁵ scan was pre-registered using a point-to-point based method as described in section 5. Here also the point distances to the ground truth (in this case the terrestrially acquired 3D laser scan) is evaluated before and after the plane-based registration process.

7. Conclusion

In this paper, we propose a registration method for man made environments that exploits the structure of the environments. Given in man-made environments parallel planes and right angles are abundantly available we⁴⁰⁵ employ point-to-plane correspondences to improve a pre-registered 3D point-cloud. We evaluate the procedure on a simulated dataset as well as on a experimentally acquired dataset with different motion profiles. In this evaluation we show that the procedure improves both datasets and

yields more human-made structure like maps. Currently not all steps in the procedure are autonomous, in particular the parameter tuning. In the future one goal is to increase the autonomy of the system. One approach is to introduce soft-locks for the optimization dimensions. I.e., instead of locking the some dimensions entirely from being used for optimization, adding weighting factors based on the dynamics of the system that encode which noise source is more likely.

Acknowledgement

Formulate these: ESA funding (?), elite netzwerk bayern (?), cylon floatsat group

References

- [1] V. V. Lehtola, J.-P. Virtanen, M. T. Vaaja, H. Hyppä, A. Nüchter, Localization of a Mobile Laser Scanner via Dimensional Reduction, *ISPRS Journal of Photogrammetry and Remote Sensing (JPRS)* 121 (2016) 48–59. doi:10.1016/j.isprsjprs.2016.09.004.
URL <https://robotik.informatik.uni-wuerzburg.de/telematics/download/jprs2016.pdf>
- [2] D. Borrmann, S. Jörissen, A. Nüchter, RADLER - A RADial LasER Scanning Device, 2020, pp. 655–664. doi:10.1007/978-3-030-33950-0_56.
- [3] H. A. Lauterbach, D. Borrmann, R. Heß, D. Eck, K. Schilling, A. Nüchter, Evaluation of a backpack-mounted 3d mobile scanning system, *Remote Sensing* 7 (10) (2015) 13753–13781. doi:10.3390/rs71013753.
URL <https://www.mdpi.com/2072-4292/7/10/13753>
- [4] B. Dynamics, Spot robot (2021).
URL <https://www.bostondynamics.com/spot>
- [5] P. Fankhauser, M. Bloesch, M. Hutter, Probabilistic terrain mapping for mobile robots with uncertain localization 3 (2018) 3019–3026. doi:10.1109/LRA.2018.2849506.
- [6] A. P. Rossi, F. Maurelli, V. Unnithan, H. Dreger, K. Matthevos, N. Pradhan, D.-A. Corbeanu, R. Pozzobon, M. Massironi, S. Ferrari, C. Pernechele, L. Paoletti, E. Simioni, P. Maurizio, T. Santagata, D. Borrmann, A. Nüchter, A. Bredenbeck, J. Zevering, F. Arzberger, C. A. R. Mantilla, Daedalus - descent and exploration in deep autonomy of lava underground structures, *Tech. Rep.* 21, Institut für Informatik (2021).
- [7] J. Guo, X. Chen, S. Guo, J. Xu, Study on map construction of spherical robot based on statistical filtering, in: 2020 IEEE International Conference on Mechatronics and Automation (ICMA), 2020, pp. 1269–1274. doi:10.1109/ICMA49215.2020.9233654.
- [8] A. Nüchter, K. Lingemann, J. Hertzberg, H. Surmann, 6D SLAM – 3D Mapping Outdoor Environments, *Journal of Field Robotics (JFR)*, Special Issue on Quantitative Performance Evaluation of Robotic and Intelligent Systems 24 (8–9) (2007) 699–722. doi:10.1002/rob.20209.
URL <https://robotik.informatik.uni-wuerzburg.de/telematics/download/jfr2007.pdf>
- [9] D. Borrmann, J. Elseberg, K. Lingemann, A. Nüchter, J. Hertzberg, Globally consistent 3d mapping with scan matching, *Journal Robotics and Autonomous Systems (JRAS)* 56 (2) (2008) 130–142. doi:10.1016/j.robot.2007.07.002.
URL <https://robotik.informatik.uni-wuerzburg.de/telematics/download/ras2007.pdf>
- [10] J. Zhang, S. Singh, Loam: Lidar odometry and mapping in real-time, 2014. doi:10.15607/RSS.2014.X.007.

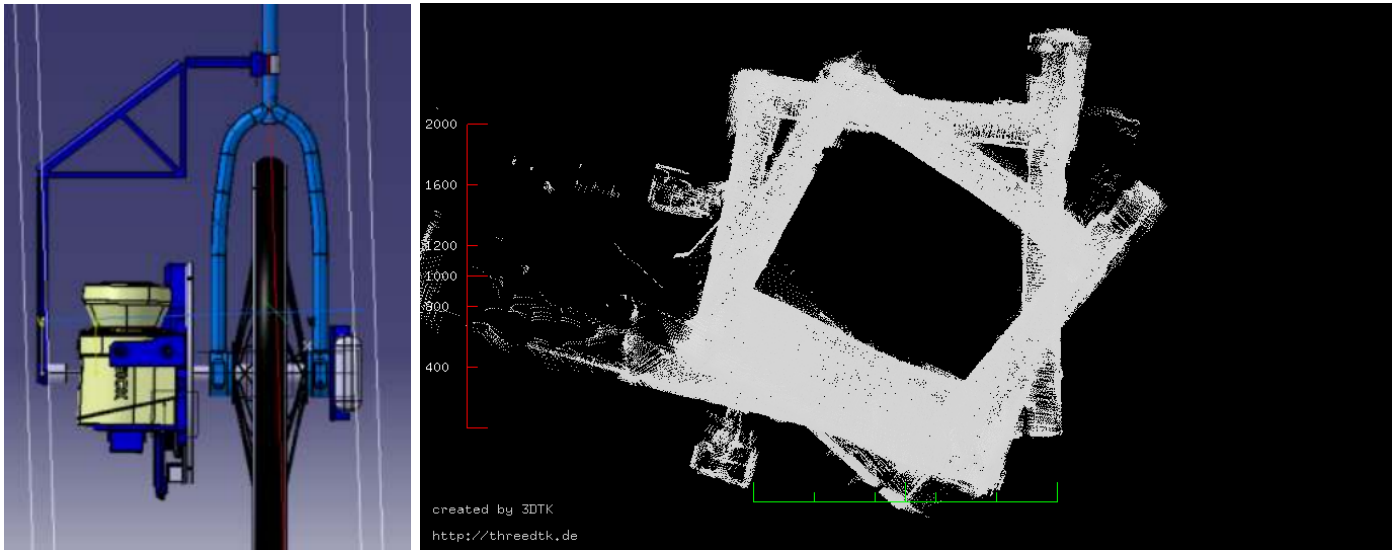


Figure 3: Data acquisition using the RADLER system. Left: System setup (courtesy of Borrmann [2]). Right: Unprocessed resulting point cloud.



Figure 4: Reference 3D point cloud acquired with a RIEGL 3D terrestrial laser scanner (top left). The 3D point cloud acquired by the test sphere after the rigid registration (bottom left) and a picture of the test setup (right).

- 410 [11] D. Droschel, S. Behnke, Efficient continuous-time slam for 3d
lidar-based online mapping, 2018 IEEE International Conference on Robotics and Automation (ICRA) doi:10.1109/icra.
2018.8461000.
URL <http://dx.doi.org/10.1109/ICRA.2018.8461000>
- 415 [12] P. J. Besl, N. D. McKay, A method for registration of 3-d shapes, IEEE Transactions on Pattern Analysis and Machine Intelligence 14 (2) (1992) 239–256. doi:10.1109/34.121791.
- [13] W. Förstner, K. Khoshelham, Efficient and accurate registration
of point clouds with plane to plane correspondences, in: 2017
IEEE International Conference on Computer Vision Workshops (ICCVW), 2017, pp. 2165–2173. doi:10.1109/ICCVW.2017.253.
- 420 [14] K. Favre, M. Pressigout, E. Marchand, L. Morin, A Plane-based
Approach for Indoor Point Clouds Registration, in: ICPR 2020
- 25th International Conference on Pattern Recognition, Milan
(Virtual), Italy, 2021.
URL <https://hal.archives-ouvertes.fr/hal-03108891>
- 425 [15] J. Elseberg, D. Borrmann, K. Lingemann, A. Nüchter, Non-rigid registration and rectification of 3d laser scans, in: 2010
IEEE/RSJ International Conference on Intelligent Robots and Systems, 2010, pp. 1546–1552. doi:10.1109/IROS.2010.

- 5652278.
- [16] D. Borrmann, J. Elseberg, K. Lingemann, A. Nüchter, The 3d hough transform for plane detection in point clouds: A review and a new accumulator design, 3D Research 2 (2011) 1–13.
 - [17] J. Diebel, Representing attitude: Euler angles, unit quaternions, and rotation vectors, Matrix 58 (15–16) (2006) 1–35.
 - [18] M. D. Zeiler, Adadelta: An adaptive learning rate method (2012). arXiv:1212.5701.
 - [19] Livox, Livox mid40 and mid100 (2021).
URL <https://www.livoxtech.com/mid-40-and-mid-100>

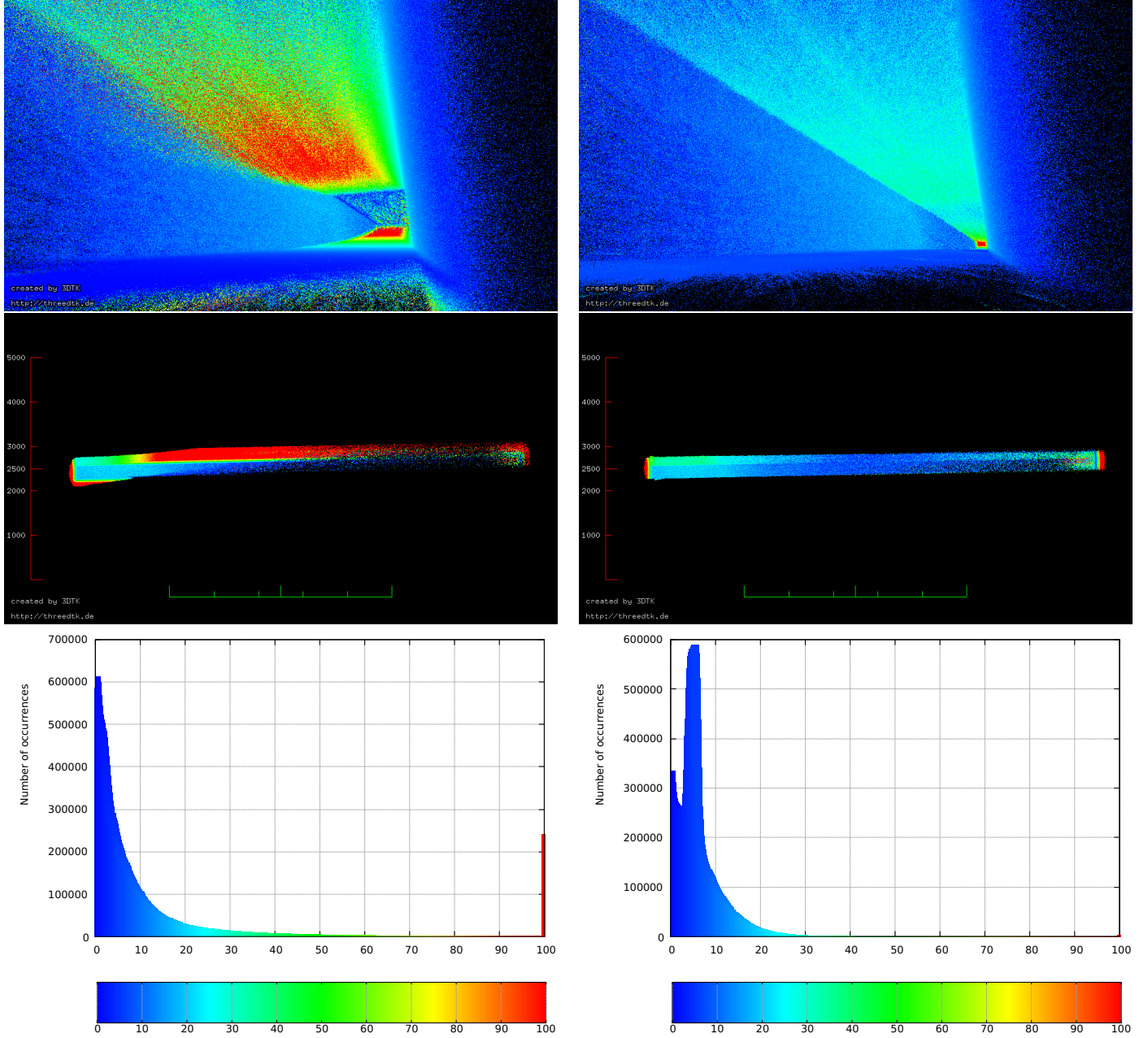


Figure 5: Evaluation of point distances before (left) and after (right) the plane based registration on a simulated dataset. A maximal distance of 2 m is set, such that all points that display a higher distance value are excluded from analysis. Further the histogram joins all values with a distance greater than 1 m into the last bucket. The top two column shows a heat map of distances while the bottom shows the corresponding histogram. The color mapping is equivalent in both. An animation of the matching process is given at here

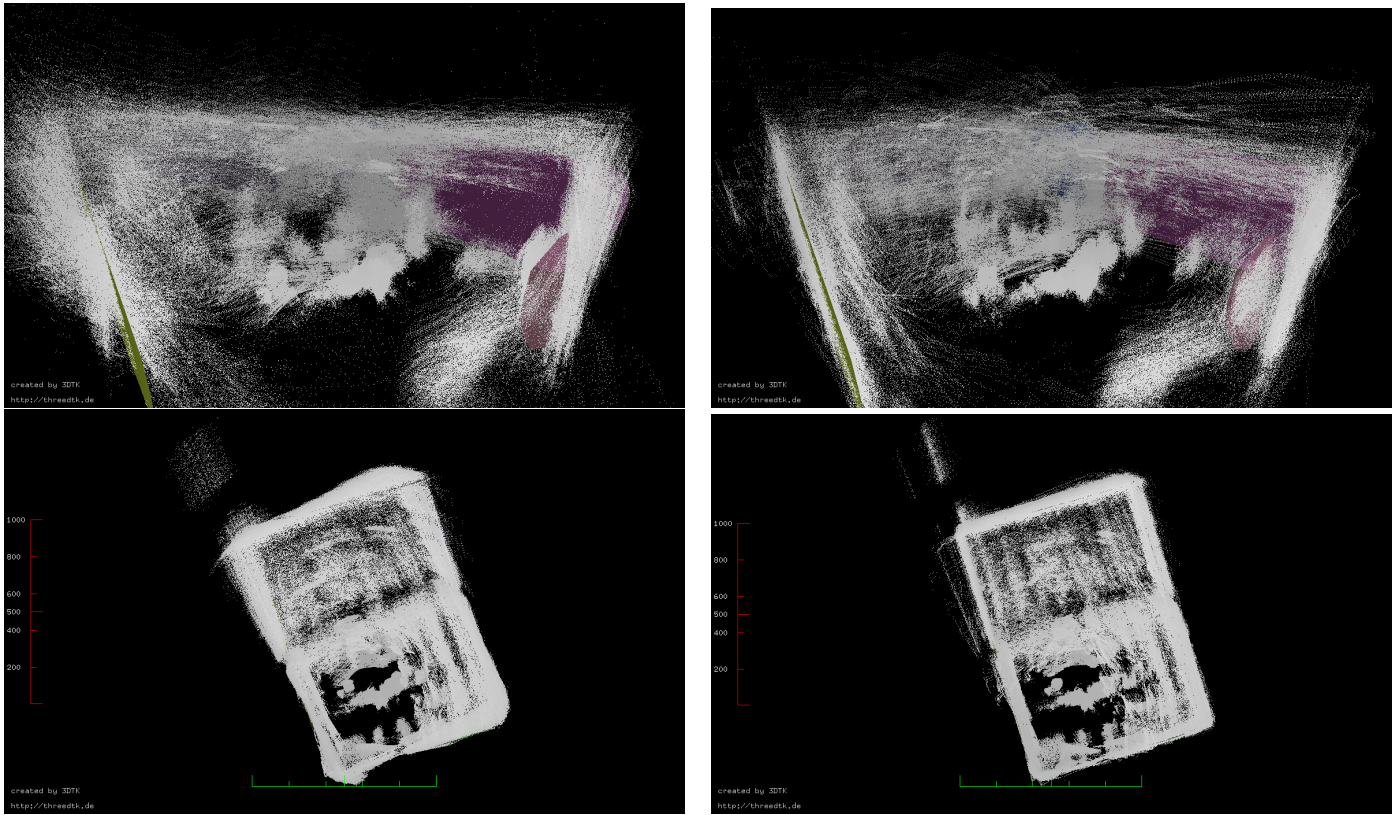


Figure 6: The point cloud acquired by the floating sphere before (left) and after (right) applying the plane based registration. View from the interior that shows the used planes (top) and a birds-eye view (bottom). An animation of the registration process is given at here.

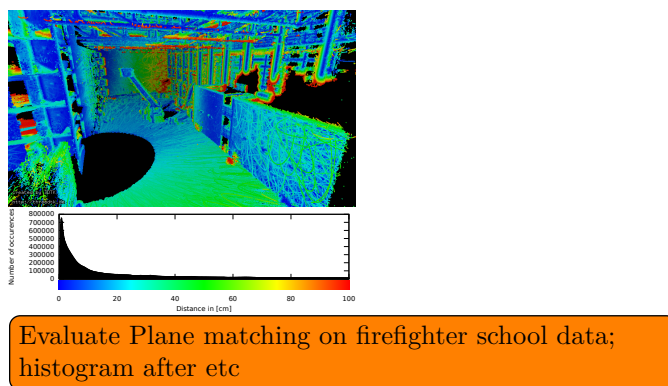


Figure 7: Evaluation of point distances before (left) and after (right) the plane based registration on a experimentally acquired dataset. A maximal distance of 5 m is set, such that all points that display a higher distance value are excluded. The left column shows a heat map of distances while the right shows the corresponding histogram. The color mapping is equivalent in both. An animation of the matching process can be seen here